Int. J. Heat Mass Transfer. Vol. 36, No. 13, pp. 3283–3298, 1993
Printed in Great Britain

0017-9310/93 \$6.00+0.00

Three-dimensional simulation of the plasma arc welding process

RUSSELL G. KEANINI†§ and BORIS RUBINSKY‡
† Department of Mechanical Engineering and Engineering Science,
University of North Carolina at Charlotte, Charlotte, NC 28223, U.S.A.
‡ Department of Mechanical Engineering, University of California, Berkeley, CA 94720, U.S.A.

(*Received* 7 *July* 1992 *and in final form* 26 *November* 1992)

Abstract—A finite element-based simulation of the plasma arc welding process is presented. The simulation determines the weld pool's three-dimensional capillary surface shape, the approximate solid–liquid phase boundary, and calculates the pool's three-dimensional flow and temperature fields. The simulation is first used to examine the effect of ambient temperature and plate speed on pool shape. Pool flow is then studied. The flow's qualitative features are primarily determined by jet shear and thermocapillarity while buoyancy is of secondary importance.

INTRODUCTION

DURING plasma arc welding, a high energy density (approximately 10^9 W m^{-2}), high velocity (100–500 m s^{-1}) plasma jet melts a small region at the junction of two metal workpieces. The jet's momentum allows the jet to penetrate completely through the weld pool forming a nearly symmetric, funnel-shaped cavity called a keyhole. As shown in Fig. 1, the weld pool extends through the workpiece and holds fast to the solid by surface tension forces [1]. During welding, metal melts in the region near the plasma jet, flows around the keyhole, and solidifies to form a weld in the rear portion of the pool.

A limited number of theoretical studies treating the PAW process have been reported, each of varying degrees of approximation, and each focusing on different aspects of the problem [2–5]. The most comprehensive model of PAW to date is Hsu and Rubinsky's [5] two-dimensional finite element simulation. This model calculates the two-dimensional (in the plane normal to the plasma jet flow axis) weld pool flow and temperature fields associated with steady travel PAW. However, this study neglects surface tension effects and simplifies the pool geometry by assuming flat upper and lower free surfaces, a keyhole of constant radius, and a non-tapering solid–liquid phase boundary.

Weld pool surface shape and thermocapillarity are important in determining the shape and mechanical properties of the final weld. A number of two-dimensional welding simulations have considered either one or both of these features [6–8]. Of the three-dimensional welding simulations which have been reported [9–13], only three have accounted for both thermocapillarity and three-dimensional capillary surface shapes [11–13].

The difficulties associated with modeling the PAW process appear to be considerably greater than those associated with most other welding processes. Most of these difficulties can be attributed to the plasma jet's passage through the pool. In particular, four significant problems can be identified.

(1) Since the pool is completely penetrated by the jet and is further deformed by jet shear, the pool surface can assume complex shapes. In addition, since the pool is relatively large (compared to electron beam and laser welding pools), the surface can sag significantly, complicating the problem further. Perhaps the greatest challenge in modeling the capillary surface lies in the fact that the surface shape depends on the pressure distributions both inside and outside the pool (as dictated by the Young–Laplace equation). Since the pressure distributions depend on the weld pool and plasma jet flow fields, which in turn depend on the surface shape, the problem is highly non-linear.

(2) The distribution and sources of shear stress on the capillary interface are non-trivial. On the upper part of the keyhole, jet and thermocapillary shear stresses presumably act in combination, with the strength of jet shear largely determined by the local plasma velocity and temperature fields [15], and the strength of thermocapillary shear determined by the local weld pool surface temperature gradient. On the lower, downward facing part of the pool, where the plasma jet no longer passes along the capillary surface, thermocapillary stresses are still extant. (We note that arc shear also occurs in GTA. However, in this case the stress magnitude is orders of magnitude smaller than in PAW and the stress direction is essentially planar, due to the nearly flat plasma–pool interface.)

(3) The nature of radiant and convective heat trans-

---

§ Author to whom correspondence should be addressed.

NOMENCLATURE

A^e	surface area of mesh element
$\mathbf{b}$	dimensionless body force, $(Gr/Re^2)\ \theta\hat{\mathbf{k}}$
f_b	height of lower free surface below reference plane
f_t	height of upper free surface, including keyhole, above reference plane
$\bar{f}_b$	initial guess for lower capillary surface height
$\bar{f}_t$	initial guess for upper capillary surface height
$\{\mathbf{f}^0\}$	vector of initially guessed surface height (upper or lower surface)
$\{\mathbf{f}^1\}$	vector of updated surface heights (upper or lower surface)
Gr	Grashof number, $g\beta L^3(T_b - T_m)/\nu^2$
$\hat{\mathbf{i}}, \hat{\mathbf{j}}, \hat{\mathbf{k}}$	unit vectors in x-, y-, z-directions
L	plate thickness
L_o	characteristic weld pool radial thickness
Ma	Marangoni number, $\lvert d\sigma/dT\rvert \Delta TL/\mu\alpha$
$\hat{\mathbf{n}}, \{\mathbf{n}\}$	unit normal vector
$\hat{\mathbf{n}}_c$	unit normal vector to a bounding surface
N	number of element nodes on linear brick (8)
N_p	center node within linear brick (1)
N_q	number of element nodes on quadratic surface element (8)
P^*	pressure
P^*_i	pressure on liquid metal side of free surface
P^*_o	external pressure on free surface
Pe_f	fluid Peclet number, $\rho_f C_{pf} LU/k_f$
Pe_s	solid Peclet number, $\rho_s C_{ps} LU/k_s$
Pr	Prandtl number, ν/α
$\mathbf{q}_s, \mathbf{q}$	dimensionless heat flux, solid and liquid regions
Ra	Rayleigh number, $g\beta(T_b - T_m)L^3/\alpha\nu$
Re	Reynolds number, UL/ν
$\hat{\mathbf{t}}, \{\mathbf{t}\}^T$	unit tangent vector
T	temperature
ΔT	$T_b - T_m$
T_b, T_m, T_o	boiling, melting ambient temperature
U	plate speed
U_p	characteristic pool velocity
u, v, w	dimensionless liquid velocity in x-, y-, z-directions
$\tilde{u}, \tilde{v}, \tilde{w}$	velocities from previous iteration (equation (24))
$\{u\}, \{v\}, \{w\}, \{\theta\}$	elemental velocity and temperature vectors in equation (23)
V^e	volume of mesh element
x, y, z	dimensionless coordinates
x_i, y_i, z_i	finite element node coordinates.

Greek symbols

α	thermal diffusivity
β	volumetric thermal expansion coefficient
γ	surface tension coefficient
γ_p	penalty constant
$\partial\Gamma_k$	line of intersection between keyhole interface and the plane of the plate's lower surface
$\partial\Gamma_b$	line of intersection between the fusion boundary and the plane of the plate's lower surface
$\partial\Gamma_t$	line of intersection between the fusion boundary and the plane of the plate's upper surface
$\delta\Omega_b$	lower capillary interface
$\delta\Omega_k$	keyhole capillary interface
$\delta\Omega_s$	upper and lower surfaces of the solid plate
$\delta\Omega_{sl}$	solid–liquid phase boundary
$\delta\Omega_t$	upper capillary interface, including keyhole
$\delta\Omega_{t'}$	upper, non-keyhole capillary interface
ε	relaxation parameter in equation (48)
ρ	density
σ	surface tension coefficient
$[\boldsymbol{\sigma}]$	stress tensor
τ_{jet}	keyhole shear stress due to plasma jet
$\phi_i, \Psi_i, \phi^{q_i}$	finite element interpolation functions.

Subscripts

α	index for free surfaces, 1 = upper surface, 2 = lower surface
α, β, γ	direction indices in equations (24)–(29)
i, j, k	node indices
x, xx, y, yy, z, zz	first and second derivatives with respect to x, y and z.

fer from the jet to the pool surface is unknown. Prior studies [3, 4] assumed that heat transfer could be adequately modeled using experimental measurements [15] of entrance flow of a plasma into a nonmelting pipe. However, since the pool interface is in motion, and since metal evaporation at the capillary interface may be significant, this approach can only be considered a first order approximation.

(4) The electromagnetic field in the vicinity of the weld pool is unknown. While it is expected that Lorentz forces are significant within the weld pool, imposing proper boundary conditions in order to simulate this effect remains problematic.

Beyond this list of difficulties, another problem arises due to the unknown location of the solid phase boundary. Solving this portion of the problem alone represents a significant challenge, since the phase boundary is determined in part by the three-dimensional flow field within the weld pool.

In this paper, we develop a finite element simulation which calculates approximate three-dimensional capillary interface and solid–liquid phase boundary shapes, and which determines the corresponding three-dimensional weld pool flow and temperature fields. The simulation is also used to calculate the associated solid phase temperature field. Due to the difficulties outlined above, several simplifying assumptions are implemented, in large part to make the simulation computationally tractable. These are described.

The study's primary purpose is to investigate the effects of plasma jet shear, thermocapillarity, and buoyancy on weld pool flow. These effects are examined under moderate Reynolds number and low Peclet number conditions. The second purpose of this work is to examine weld pool shapes under a few practical conditions. Here, pool shapes are determined as functions of plate travel speed and ambient temperature.

PROBLEM FORMULATION

Assumptions

The following simplifications are introduced, either to make the simulation computationally practicable or due to insufficient information concerning a particular aspect of the problem. Note that throughout the remainder of the paper we will refer to the interface between the plasma jet and the weld pool as the keyhole (refer to Figs. 1 and 2). As discussed below, the capillary surface will be divided into three distinct regions: an upper non-keyhole region, the keyhole, and a lower non-keyhole region.

(1) We assume that the plasma jet is columnar, having a circular cross-section at the point where it impinges on the weld pool. The assumed radius is characteristic of the jet's radius at its exit from the weld torch. In actuality, the jet spreads radially somewhat as it travels from the torch to the pool. The present assumption captures the essential physics since jet momentum remains concentrated near the flow axis.

(2) The capillary surface shapes are determined by performing one Newton–Raphson iteration on the initial surface guess. Subsequent iterations were deemed unnecessary since no surface position, in any of the cases considered, changed by more than 1% from the first iterate to the converged solution (see below). This feature reflects the fact that the initial guesses were based on experimentally observed shapes.

(3) In calculating the capillary surface shapes, pressure within the pool is assumed to be hydrostatic, and external pressure is assumed to take on one of two constant values. On the non-keyhole portions of the capillary surface, the external pressure is atmospheric, while within the keyhole, pressure assumes a slightly higher value (2000 Pa in excess of atmospheric), characteristic of the plasma pressures calculated in an earlier study [4]. The assumption of a constant in-keyhole plasma pressure is consistent with earlier calculations which indicated negligible plasma pressure variations within the keyhole [4]. A rigorous solution for the surface shape requires accurate knowledge of the dynamic pressure fields both interior and exterior to the pool. This in turn requires an expensive iterative procedure in which the non-linear three-dimensional flow and temperature fields within both the pool and plasma jet are solved several times in arriving at the final capillary surface solution. Future work which incorporates a solution for the plasma jet will focus on developing an efficient means of solving the complete coupled problem.

(4) A conduction solution, based on a guessed capillary surface shape, is used to locate the solid–liquid

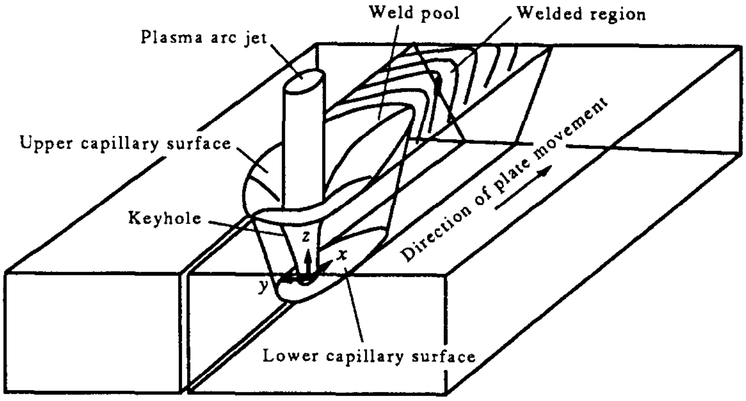

FIG. 1. Schematic of the plasma arc welding process.

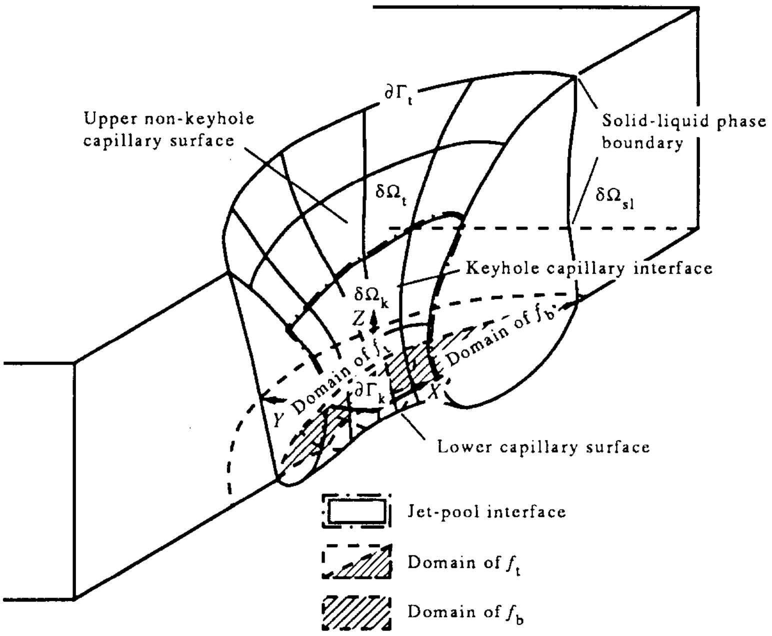

FIG. 2. Detail of the weld pool geometry.

phase boundary. We thus neglect both weld pool convection and the difference between the guessed capillary surface shape and the final shape. Since the maximum Peclet number considered in this study is 0.23, then convection will be of secondary importance in most cases. This is confirmed by the results below. Similarly, since the average difference between any guessed capillary surface position (i.e. the height above a reference plane) and the final solution averages 6%, then the error introduced in using the initial guess will not be significant.

(5) Electromagnetic forces are neglected, in part due to the lack of information concerning the in-keyhole electric field.

(6) Plasma heat transfer is assumed to occur only on the keyhole portion of pool surface. Radiative and convective heat transfer on the remainder of the pool surface and on the upper and lower surfaces of the solid plate is neglected. Similarly, evaporation from the pool is neglected. Although neglecting radiation and evaporation may introduce quantitative errors into the weld pool flow and temperature calculations, the qualitative flow features arising from jet shear, thermocapillarity, and buoyancy should not be affected. Future work which solves for the plasma jet velocity, temperature and electric fields will incorporate evaporation and radiation effects.

(7) The keyhole interface is assumed to be at the metal's boiling temperature. This assumption is consistent with boiling we have observed on the upper portion of the keyhole, and is also consistent with the 10^4 K characteristic plasma temperature that exists within the keyhole. It is not known however, whether boiling actually occurs throughout the keyhole.

(8) Plasma jet shear within the keyhole is assumed constant and on the order of the shear measured for entrance flow of a plasma into a circular pipe [15]. This assumption is employed since an earlier study [4] indicated that in-keyhole jet shear is independent of plasma mass flow rate.

(9) Consistent with the low heats of fusion which characterize most metals, latent heat effects are neglected [5, 16–18].

(10) All thermophysical properties, save surface tension and thermal conductivity, in both the solid and liquid phases are assumed constant, and are representative of AISI 304 stainless steel. Surface tension is assumed to vary linearly with temperature [9, 11, 12]. While different conductivities are used in the solid and liquid regions [9, 11, 12], each of the other properties are assumed to be equal in each phase [9, 11, 12] (see Table 1).

(11) The weld pool flow is assumed Newtonian, incompressible, quasi-steady, and laminar.

Model

We assume that the problem is symmetric about the plane $y = 0$ and thus perform our calculations in the region where $y \geqslant 0$. We fix a coordinate system to the moving jet, with the origin placed at the bottom of the keyhole (refer to Figs. 1 and 2).

Given the assumptions listed above, the non-dimensionalized Navier–Stokes equations are given by

$$uu_x + vu_y + wu_z = -\frac{P_x^*}{\rho U^2} + \frac{1}{Re}(u_{xx} + u_{yy} + u_{zz}) + \mathbf{b}_x \tag{1}$$

Table 1. Thermal physical properties, dimensionless numbers and parameters

$\beta = 10^{-4}\,\mathrm{C}^{-1}$
$C_p = 700\,\mathrm{J\,kg^{-1}\,{}^{\circ}C^{-1}}$
$\gamma_p = 10^7$
$|\mathrm{d}\sigma/\mathrm{d}T| = 0.0003\,\mathrm{kg\,s^{-2}\,{}^{\circ}C^{-1}}$
$k_s = 25\,\mathrm{W\,m^{-1}\,{}^{\circ}C^{-1}}$
$k_f = 30\,\mathrm{W\,m^{-1}\,{}^{\circ}C^{-1}}$
$L = 0.01\,\mathrm{m}$
$L_o = 0.003\,\mathrm{m}$
$\mu = 10^{-3}\,\mathrm{kg\,m^{-1}\,s^{-1}}$
$\rho_f, \rho_s = 7200\,\mathrm{kg\,m^{-3}}$
$\sigma = 15\,\mathrm{N\,m^{-1}}$
$T_m = 1400^{\circ}\mathrm{C}$
$T_b = 2800^{\circ}\mathrm{C}$
$\tau_{jet} = 140\,\mathrm{N\,m^{-2}}$
$Re = 10$
$Pe = 0.23$
$10^3 < Ra < 10^5$

$$uv_x + vv_y + wv_z = -\frac{P_y^*}{\rho U^2} + \frac{1}{Re}(v_{xx} + v_{yy} + v_{zz}) + \mathbf{b}_y \tag{2}$$

$$uw_x + vw_y + ww_z = -\frac{P_z^*}{\rho U^2} + \frac{1}{Re}(w_{xx} + w_{yy} + w_{zz}) + \mathbf{b}_z \tag{3}$$

$$u_x + v_y + w_z = 0 \tag{4}$$

where Re is the Reynolds number, $\mathbf{b}$ is the non-dimensional body force, and P^* is the dimensional pressure. Velocities are scaled to the plate travel speed, U, while lengths are scaled to the plate thickness, L.

It is important to note that a very thin thermocapillary-induced boundary layer is likely to exist along the non-keyhole portions of the capillary surface. Referring to Ostrach [19], the relevant boundary layer velocity scale and thickness are

$$U_s = \frac{|\mathrm{d}\sigma/\mathrm{d}T|(T_b - T_m)v}{\mu^2 L}$$

and

$$\delta = \frac{Lv}{L_o U_s}.$$

Using the values in Table 1, we find that $U_s = \mathrm{O}(1\ \mathrm{m\ s^{-1}})$ and $\delta = \mathrm{O}(10^{-5}\ \mathrm{m})$ (so that $\delta/L_o = \mathrm{O}(10^{-2})$). The corresponding Reynolds number based on U_s and L is on the order of 10^4, indicating that the layers may be turbulent. No attempt was made to resolve these boundary layers; rather, due to the approximate nature of the stress and thermal boundary conditions, the calculations were confined to the non-boundary layer core region within the pool (comprising on the order of 99% of the pool's volume). As argued below (see Results), due to the requirement that surface tension maintains the pool against jet shear, jet impingement, pool weight and flow-induced dynamic pressure, the velocity scale within the core is only on the order of 1 mm $\mathrm{s^{-1}}$–1 cm $\mathrm{s^{-1}}$ (consistent with the velocity scale used above). Clearly, future work which incorporates accurate boundary conditions will require accounting of the thermocapillary and jet shear boundary layers.

The Boussinesq approximation is employed so that for the coordinate system shown in Fig. 2, $\mathbf{b}$ is given by

$$\mathbf{b} = \frac{Gr}{Re^2}\theta\mathbf{k} \tag{5}$$

where θ is the non-dimensional liquid temperature

$$\theta = \frac{(T - T_m)}{(T_b - T_m)}$$

and $Gr = g\beta(T_b - T_m)L^3/v^2$ is the Grashof number. The non-dimensional energy equation is given as

$$u\theta_x + v\theta_y + w\theta_z = \frac{1}{Pe_f}(\theta_{xx} + \theta_{yy} + \theta_{zz}) \tag{6}$$

where $Pe_f = Re\,Pr$ is the fluid Peclet number. Heat conduction in the solid region is governed by

$$\theta_x^s = \frac{1}{Pe_s}(\theta_{xx}^s + \theta_{yy}^s + \theta_{zz}^s) \tag{7}$$

where θ^s is the non-dimensional solid temperature

$$\theta^s = \frac{(T - T_o)}{(T_m - T_o)}$$

and $Pe_s = UL/\alpha_s$ is the solid Peclet number. Note, the non-dimensional velocity multiplying θ_x^s is 1. The Young–Laplace equation, which describes the surface curvature of an interface between two immiscible fluids, can be written in non-dimensional form as

$$\nabla_H \cdot \hat{\mathbf{n}} + K = 0. \tag{8}$$

Here, $\hat{\mathbf{n}}$ is the local unit normal to the interface, K is the non-dimensional pressure difference across the interface, and

$$\nabla_H = \frac{\partial}{\partial x}\hat{\mathbf{i}} + \frac{\partial}{\partial y}\hat{\mathbf{j}} \tag{9}$$

is the divergence operator in the horizontal plane (refer to Fig. 2). K is given as

$$K = L\frac{(P_o^* - P_i^*)}{\sigma} \tag{10}$$

where $P_o^* - P_i^*$ is the local pressure difference across the interface and σ is the surface tension coefficient. For the problem considered here, the weld pool's capillary interface is divided into two adjoining surfaces. The first surface, which will be referred to as the upper surface, $\delta\Omega_t$, is assumed to extend from a half-circle lying at the bottom of the keyhole (in the plane $z = 0$) to the solid–liquid phase boundary on the workpiece's upper surface ($z = 1$). The second, or lower surface, $\delta\Omega_b$, extends from the same half-circle to the workpiece's bottom solid–liquid phase boundary (on $z = 0$). See Fig. 2. The assumption of a half-circle (i.e. circular keyhole) at the intersection of the two surfaces was guided by experimentally determined keyhole shapes [3, 14].

Assuming that each surface has no folds, then each can be described as a function of Cartesian coordinates x and y

$$f_t = f_t(x, y) \tag{11a}$$

$$f_b = f_b(x, y) \tag{11b}$$

where f_t is the height of the upper surface ($\delta\Omega_t$) above the reference plane ($z = 0$) and f_b is the distance from the reference plane to the lower capillary interface ($\delta\Omega_b$). The domain of f_t lies in the plane $z = 0$ and is bounded by the half-circle at the keyhole, the x-axis, and by the vertical projection of $\partial\Gamma_t$ onto the plane $z = 0$ (where $\partial\Gamma_t$ is the line of intersection between the fusion boundary and the upper capillary surface). Refer to Fig. 2. The domain of f_b is similarly defined, except that the intersection line between the fusion boundary and the lower capillary surface ($\partial\Gamma_b$) replaces the boundary projected from $\partial\Gamma_t$.

The unit normal in (8) can now be expressed as

$$\hat{\mathbf{n}}_\alpha = \frac{-f_{\alpha,x}\hat{\mathbf{i}} - f_{\alpha,y}\hat{\mathbf{j}} + \hat{\mathbf{k}}}{(1 + f_{\alpha,x}^2 + f_{\alpha,y}^2)^{1/2}} \tag{12}$$

so that inserting (12) into (8) leads to

$$\frac{-f_{\alpha,xx}(1 + f_{\alpha,x}^2) - f_{\alpha,yy}(1 + f_{\alpha,x}^2) + 2f_{\alpha,x}f_{\alpha,y}f_{\alpha,xy}}{(1 + f_{\alpha,x}^2 + f_{\alpha,y}^2)^{3/2}} + K = 0$$

$$\alpha = 1, 2. \tag{13}$$

Here, subscript α denotes either the upper or lower surface.

Boundary conditions

The no-slip condition applies on the solid–liquid boundary so that the fluid velocity on this surface is just the plate velocity

$$\mathbf{u} \cdot \hat{\mathbf{n}} = 1 \quad \text{on } \delta\Omega_{sl}. \tag{14}$$

The temperature on this surface is the melting temperature

$$\theta = 0 \quad \text{on } \delta\Omega_{sl}. \tag{15}$$

Within the keyhole, the shear between the plasma jet and the weld pool is given by

$$\{\mathbf{t}\}^T[\sigma]\{\mathbf{n}\} = \tau_{jet} \quad \text{on } \delta\Omega_k \tag{16a}$$

while on the non-keyhole portions of the free surface the tangential stress is due to thermally induced surface tension gradients

$$\{\mathbf{t}\}^T[\sigma]\{\mathbf{n}\} = \frac{d\sigma}{dT}\nabla T \cdot \hat{\mathbf{t}} \quad \text{on } \delta\Omega_t, \delta\Omega_b. \tag{16b}$$

In equation (16), $[\sigma]$ is the viscous stress tensor ($\sigma_{ij} = \mu(u_{i,j} + u_{j,i})$), $\hat{\mathbf{t}}$ and $\{\mathbf{t}\}$ are the unit tangent vector, and $\{\mathbf{n}\}$ is the unit normal. As mentioned above, the temperature on the keyhole interface is assumed to be the metal's boiling point

$$\theta = 1 \quad \text{on } \delta\Omega_k. \tag{17}$$

On the symmetry plane, $y = 0$, the velocity in the y-direction vanishes, as do all derivatives with respect to y

$$v = 0; \quad \frac{\partial \mathbf{u}}{\partial y} = 0; \quad \frac{\partial \theta}{\partial y} = 0; \quad \frac{\partial \theta^s}{\partial y} = 0 \quad \text{at } y = 0. \tag{18}$$

The kinematic condition that no liquid metal crosses the capillary surface is enforced by

$$\mathbf{u} \cdot \hat{\mathbf{n}} = 0 \quad \text{on } \delta\Omega_t, \delta\Omega_b. \tag{19}$$

The upper and lower solid surfaces are assumed adiabatic

$$\frac{\partial \theta^s}{\partial z} = 0 \quad \text{on } \delta\Omega_s \tag{20a}$$

as are the non-keyhole portions of the capillary surface

$$\frac{\partial \theta}{\partial n} = 0 \quad \text{on } \delta\Omega_t, \delta\Omega_b. \tag{20b}$$

One further condition completes the solid conduction problem: at points far removed from the weld the solid temperature approaches the temperature of the surroundings

$$\theta^s \to 0 \quad \text{as } \mathbf{r} \to \infty. \tag{21}$$

We note that the temperature on the solid–liquid interface is the melt temperature

$$\theta^s = 1 \quad \text{on } \delta\Omega_{sl}. \tag{22}$$

Boundary conditions on the capillary surface are discussed in the next section.

Finite elements formulation

The continuum formulation described in equations (1)–(21) is recast into a form suitable for numerical solution using the Galerkin finite element method. The penalty method is employed here, largely due to its increased computational efficiency over the pressure–velocity formulation [20]. As discussed elsewhere [21], the penalty method replaces P with $-\gamma_p\nabla \cdot \mathbf{u}$ so that pressure is removed from the momentum equations. In addition, since the continuity equation (4) is essentially satisfied by choosing γ_p large enough (4) does not have to be considered in the finite element formulation. Applying Galerkin's method to the stress–divergence form of the Navier–Stokes equations then yields a set of weighted residual equations [21]

$$\begin{bmatrix} [K^{11}][K^{12}][K^{13}][K^{14}] \\ [K^{21}][K^{22}][K^{23}][K^{24}] \\ [K^{31}][K^{32}][K^{33}][K^{34}] \\ [K^{41}][K^{42}][K^{43}][K^{44}] \end{bmatrix} \begin{Bmatrix} \{u\} \\ \{v\} \\ \{w\} \\ \{\theta\} \end{Bmatrix} = \begin{Bmatrix} \{F^1\} \\ \{F^2\} \\ \{F^3\} \\ \{F^4\} \end{Bmatrix}. \tag{23}$$

The sub-matrices $[K]$ are given by

$$K_{ij}^{\alpha\beta} = \int_{V^c} \Bigg[\phi_i(\tilde{u}\phi_{j,x} + \tilde{v}\phi_{j,y} + \tilde{w}\phi_{j,z}) + \frac{1}{Re}(2\phi_{i,x_\alpha}\phi_{j,x_\alpha} + \phi_{i,x_\beta}\phi_{j,x_\beta} + \phi_{i,x_\gamma}\phi_{j,x_\gamma}) + \gamma_p(\phi_{i,x_\alpha}\phi_{j,x_\alpha}) \Bigg] \mathrm{d}V$$

$$(\alpha = \beta\,; \alpha, \beta, \gamma = 1, 2, 3\,; i, j = 1, 2, \ldots, N) \quad (24)$$

$$K_{ij}^{\alpha\beta} = \int_{V^c} \left[\frac{1}{Re}(\phi_{i,x_\beta}\phi_{j,x_\alpha}) + \gamma_p(\phi_{i,x_\alpha}\phi_{j,x_\beta}) \right] \mathrm{d}V$$

$$(\alpha \neq \beta\,; \alpha, \beta, \gamma = 1, 2, 3\,; i, j = 1, 2, \ldots, N) \quad (25)$$

$$F_i^\alpha = \int_{A^c} \phi_i \tau_\alpha \, \mathrm{d}A \quad (\alpha = 1, 2, 3\,; i = 1, 2, \ldots, N) \quad (26)$$

where $\tilde{u}$, $\tilde{v}$, and $\tilde{w}$ are the velocities calculated in the previous iteration. Equation (26) applies to elements having a face on a capillary surface. For elements having a face lying on a *non-keyhole* capillary surface

$$\tau_\alpha = \frac{Ma}{Re^2\,Pr} \nabla\theta \cdot \hat{\mathbf{t}}t_\alpha \quad (27)$$

while elements with faces on the *keyhole* interface have

$$\tau_\alpha = \frac{\tau_{\mathrm{jet}}}{\rho U^2} t_\alpha. \quad (28)$$

$Ma = |\mathrm{d}\sigma/\mathrm{d}T|\Delta Tl/\mu\alpha$ is the Marangoni number and t_α is the α component of $\hat{\mathbf{t}}$. Interior elements having no external faces have force vectors given by

$$F_i^\alpha = \frac{Ra}{Pe_f} \int_{V^c} (\phi_i \phi_j \tilde{T}_j) \, \mathrm{d}V \quad (29)$$

where $\tilde{T}_j$ is the nodal temperature from the previous iteration, and $Ra = g\beta(T_b - T_m)L^3/\alpha\nu$ is the Rayleigh number. $[K^{44}]$ is the only non-zero sub-matrix in the fourth row and column of the elemental stiffness matrix (23) and is given by

$$K_{ij}^{44} = \int_{V^c} \left[\phi_i(\tilde{u}\phi_{j,x} + \tilde{v}\phi_{j,y} + \tilde{w}\phi_{j,z}) + \frac{1}{Pe_f}(\phi_{i,x}\phi_{j,x} + \phi_{i,y}\phi_{j,y} + \phi_{i,z}\phi_{j,z}) \right] \mathrm{d}V \quad (30)$$

where i and j run from 1 to N. The load term $\{F^4\}$ is given as

$$F_i^4 = \frac{1}{Pe_f} \int_{A^c} (\phi_i \mathbf{q} \cdot \hat{\mathbf{n}}) \, \mathrm{d}A \quad (31)$$

where $\mathbf{q} = \nabla\theta$ is the dimensionless heat flux. The set of equations (23)–(31) are coupled and non-linear, and so must be solved iteratively. As described in the following section, a successive substitution technique is employed.

The finite element formulation of the solid conduction equation (7) is given by

$$[K^s]\{\theta^s\} = \{F^s\} \quad (32)$$

where

$$K_{ij}^s = \int_{V^c} \left[\phi_i \phi_{j,x} + \frac{1}{Pe_s}(\phi_{i,x}\phi_{j,x} + \phi_{i,y}\phi_{j,y} + \phi_{i,z}\phi_{j,z}) \right] \mathrm{d}V \quad (33)$$

and

$$F_i^s = \frac{1}{\rho C_p U \Delta T^s} \int_{A^c} (\phi_i \mathbf{q}_s \cdot \hat{\mathbf{n}}) \, \mathrm{d}A \quad (34)$$

and where $\Delta T^s = T_m - T_o$, $\mathbf{q}_s = \nabla\phi_s$, and i and j again run from 1 to N.

Application of the Galerkin procedure to the Young–Laplace equation (8) yields [22]

$$\int_{A^c} (\phi_i^q(\nabla_H \cdot \hat{\mathbf{n}} + K)) \, \mathrm{d}A = 0. \quad (35)$$

Employing the two-dimensional version of the divergence theorem and using equation (13) leads to [22]

$$[K^{\mathrm{surf}}]\{f\} = \{F^{\mathrm{surf}}\} \quad (36)$$

where

$$K_{ij}^{\mathrm{surf}} = \int_{A^c} \left(\phi_i^q K + \frac{\phi_{i,x}^q \phi_{j,x}^q + \phi_{i,y}^q \phi_{j,y}^q}{(1 + \bar{f}_{,x}^2 + \bar{f}_{,y}^2)^{1/2}} \right) \mathrm{d}A \quad (37)$$

and

$$F_i^{\mathrm{surf}} = -\int_{L^c} (\phi_i^{ql} \hat{\mathbf{n}} \cdot \hat{\mathbf{n}}_c) \, \mathrm{d}l. \quad (38)$$

$\bar{f} = \bar{f}(x, y)$ is the first guess for f (where the subscript denoting upper and lower surfaces has been suppressed for clarity) and ϕ_i^{ql} is an interpolation function for a quadratic line element. Equation (38) is a line integral evaluated on $\partial\Gamma_t$ and $\partial\Gamma_k$ in the solution for f_t (upper surface) and on $\partial\Gamma_b$ and $\partial\Gamma_k$ in the solution for f_b (lower surface). $\hat{\mathbf{n}}_c$ is a unit normal vector to the solid–liquid phase boundary, evaluated on the curve $\partial\Gamma_t$ in the solution for f_t and on $\partial\Gamma_b$ in the solution for f_b. Along $\partial\Gamma_k$, $\hat{\mathbf{n}}_c$ is directed in the positive z-direction in the solution for f_t and in the negative z-direction in the solution for f_b. $\hat{\mathbf{n}}$ is the unit normal to f_t ($\alpha = 1$) of f_b ($\alpha = 2$).

The boundary conditions used to solve (36) for the upper capillary surface are

$$f_t(z = 0) = 0 \quad \text{on } \partial\Gamma_k \quad (39)$$

and

$$f_t(z = 1) = 1 \quad \text{on } \partial\Gamma_t. \quad (40)$$

Similarly, boundary conditions used in the lower surface solution are

$$f_b(z = 0) = 0 \quad \text{on } \partial\Gamma_k \quad (41)$$

and

$$f_b(z=0)=0 \quad \text{on } \partial\Gamma_b. \tag{42}$$

Computer code

The program first calculates the solid temperature field using an assumed capillary surface shape. The solid temperature solution is obtained in the standard fashion. Each elemental stiffness matrix and load vector is calculated according to equation (7) and then assembled into a global stiffness matrix and load vector. Two-point Gaussian quadrature is used to calculate all stiffness and load terms. Boundary conditions are imposed at the appropriate nodes and the corresponding rows and columns are condensed out of the global stiffness matrix. The condensed system of equations is then solved using *LU* decomposition.

The solid temperature solution is fed to a mesh generator which constructs an initial mesh within the fluid region. The initial mesh boundaries are then calculated using the melt isotherm and the guessed capillary interface. The upper and lower capillary surfaces are then calculated using one Newton–Raphson iteration, as prescribed by [22]

$$\{\mathbf{f}^1\} = \{\mathbf{f}^0\} - \{\mathbf{df}^0\} \tag{43}$$

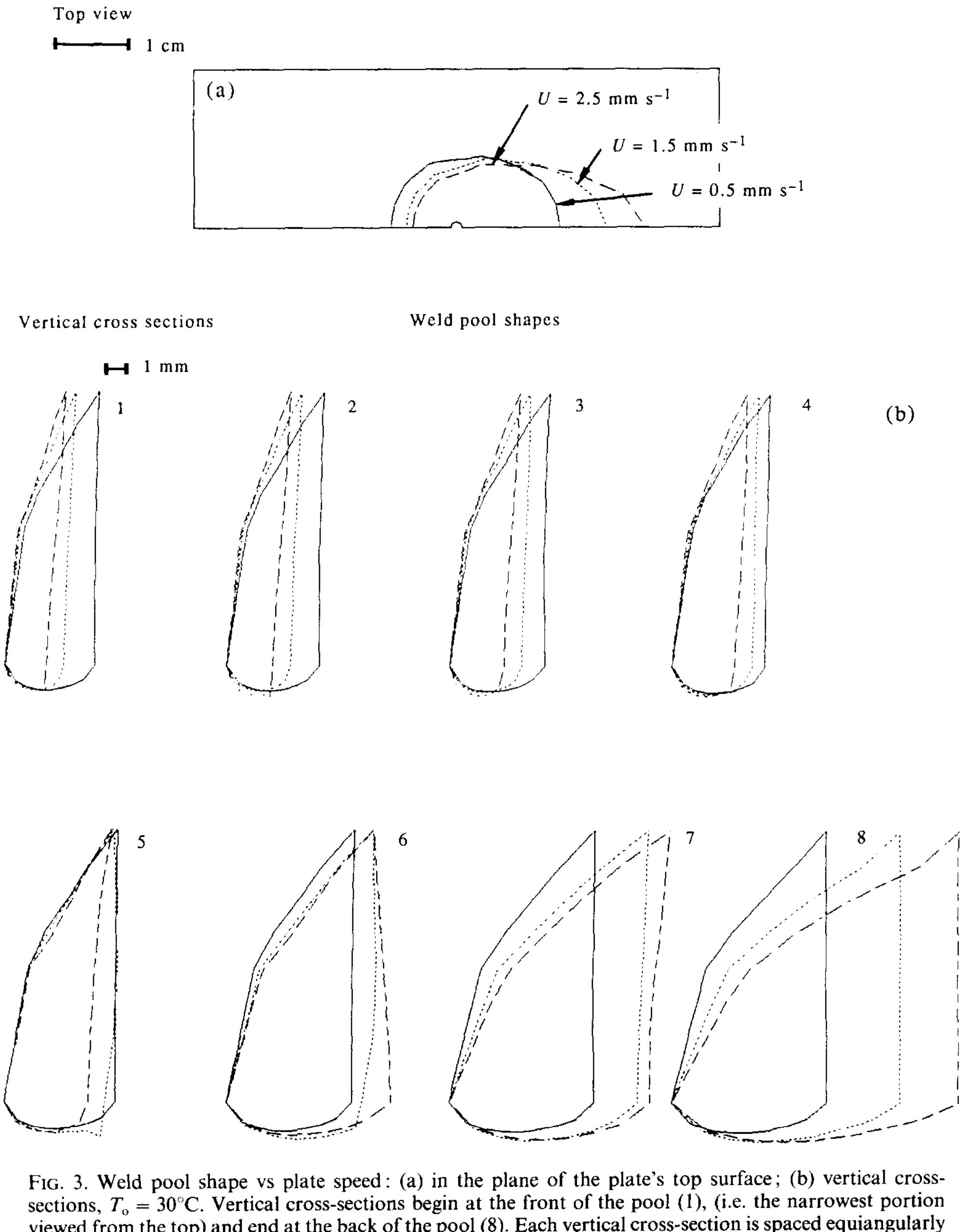

FIG. 3. Weld pool shape vs plate speed: (a) in the plane of the plate's top surface; (b) vertical cross-sections, T_0 = 30°C. Vertical cross-sections begin at the front of the pool (1), (i.e. the narrowest portion viewed from the top) and end at the back of the pool (8). Each vertical cross-section is spaced equiangularly about the z-axis (refer to Figs. 1 and 2). The same numbering scheme is used in Figs. 4–6 and 8.

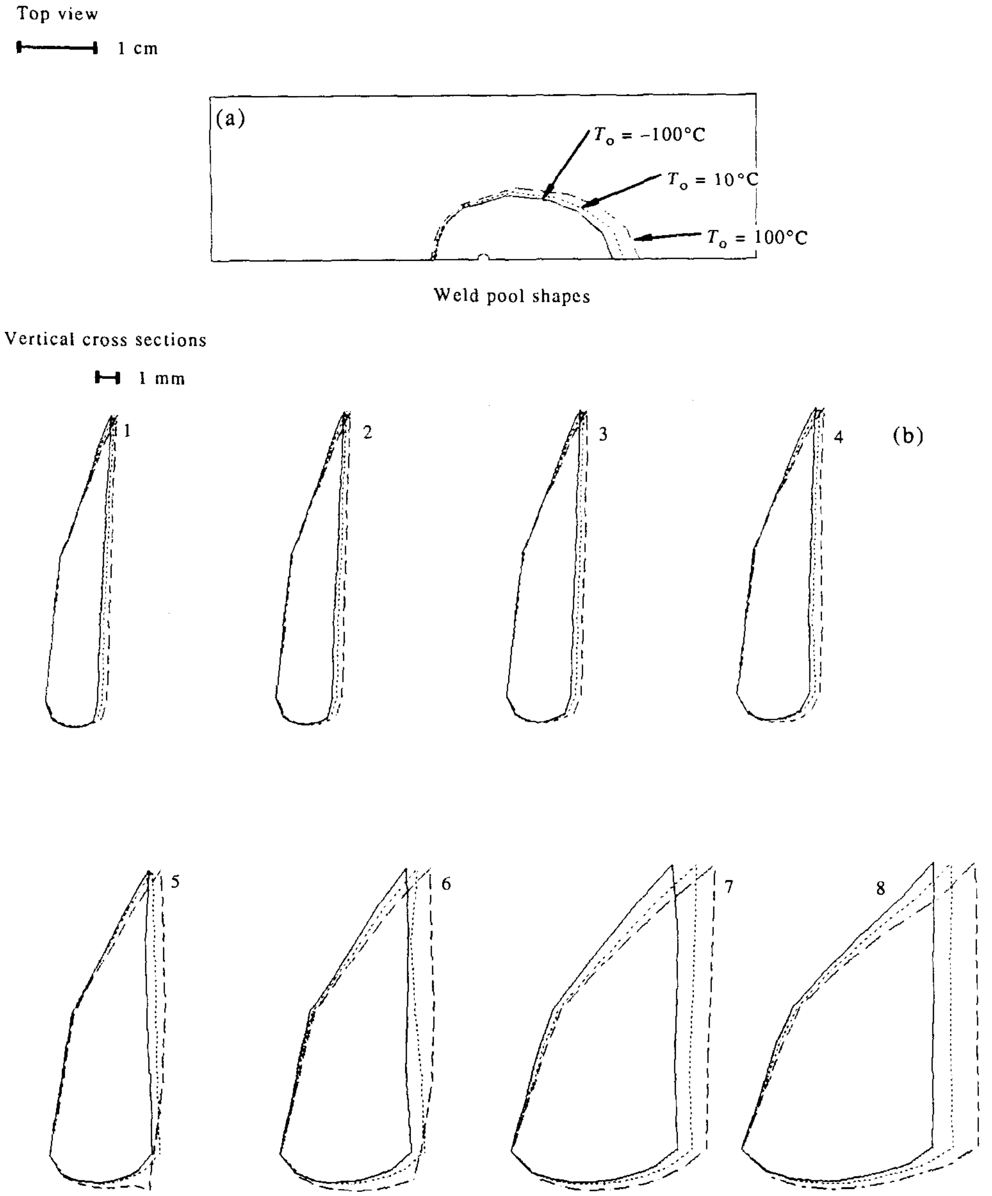

FIG. 4. Weld pool shape vs ambient temperature: (a) in the plane of the plate's top surface; (b) vertical cross-sections. $U = 1.5$ mm s^{-1}.

where $\{\mathbf{f}^1\}$ is the vector of updated surface heights (upper or lower), $\{\mathbf{f}^0\}$ is the vector of initial heights, and $\{\mathrm{d}\mathbf{f}^0\}$ is the change in $\{\mathbf{f}^0\}$. $\{\mathrm{d}\mathbf{f}^0\}$ is determined by solving

$$[\mathbf{J}^0]\{\mathrm{d}\mathbf{f}^0\} = \{\mathbf{R}^0\} \tag{44}$$

where the components of $\{\mathbf{R}^0\}$ are given by

$$R_i^0 = \int_{A^c} \left(\phi_i^q K + \frac{\phi_{i,x}^q \bar{f}_{,x} + \phi_{i,y}^q \bar{f}_{,y}}{(1+\bar{f}_{,x}^2+\bar{f}_{,y}^2)^{1/2}} \right) \mathrm{d}A + \int_{L^c} (\phi_i^{q1} \hat{\mathbf{n}} \cdot \hat{\mathbf{n}}_c)\, \mathrm{d}l \tag{45}$$

and where

$$J_{ij} = \int_\Omega \left[\frac{\phi_{i,x}^q \phi_{j,x}^q + \phi_{i,y}^q \phi_{j,y}^q}{(1+\bar{f}_x^2+\bar{f}_y^2)^{1/2}} - \frac{(\phi_{i,x}^q \bar{f}_x + \phi_{i,y}^q \bar{f}_y)(\phi_{j,x}^q \bar{f}_x + \phi_{j,y}^q \bar{f}_y)}{(1+\bar{f}_x^2+\bar{f}_y^2)^{3/2}} \right] \mathrm{d}A. \tag{46}$$

Equation (44) is solved by the same set of operations used to solve for the solid temperature field and the solution is added to the initial guess for f to give the final computed shapes.

Note, as explained above, one Newton iteration was sufficient for calculating the capillary surface shape. This simplified approach was verified in two ways for all of the shape solutions reported in this

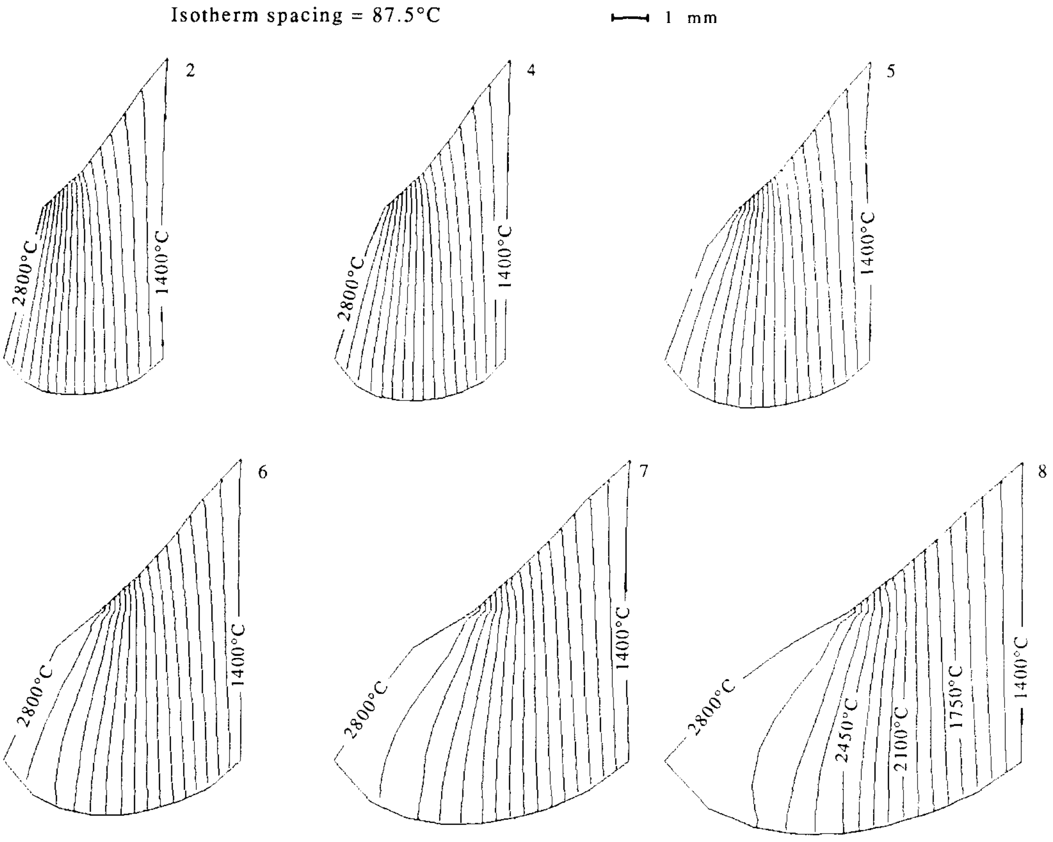

FIG. 5. Weld pool temperature distribution. $U = 1.5$ mm s^{-1}, $T_o = 30°\mathrm{C}$.

paper. First, Newton iterations were performed until the following convergence criterion was satisfied:

$$\sum_{i=1}^{N_s} [(f_i^{k+1} - f_i^k)/f_i^k]^2 < \varepsilon_s \tag{47}$$

where f_i^k is the ith surface height, k is the iteration number, N_s is the number of surface nodes, and $\varepsilon_s = 10^{-4}$. The calculations were repeated using a simple successive substitution method. In each case, the converged solutions were the same. More importantly, the maximum change in any nodal f value from $k = 1$ to convergence was always less than 1%, and generally on the order of 0.1%. Typically, convergence occurred following the second Newton iteration and following the third successive substitution. Five-point Gaussian quadrature was employed for these calculations.

Once the upper and lower capillary surfaces are calculated, the mesh in the fluid region is adjusted, and calculation of the weld pool velocity and temperature fields commences. The procedure follows that described by Reddy [21] and entails solving the momentum and energy equations for a set of increasing Reynolds and Peclet numbers. Beginning with relatively low values for *Re* and *Pe*, all non-specified velocity components and temperatures are initially set to zero. For given values of *Re* and *Pe*, an iterative procedure is employed in which solutions from the first and subsequent iterations are introduced into the nonlinear terms of the momentum and energy equations. Iterations continue until the maximum relative change in any variable at any node is less than a specified tolerance, 0.01 for the calculations described here. Once a converged solution is obtained, *Re* and *Pe* are increased and the preceding converged solution is used as a first guess for the next set of calculations. Two-point Gaussian quadrature is used for all load terms and all stiffness terms not associated with the penalty parameter. Stiffness terms multiplied by γ_p are integrated using one point quadrature [21]. Convergence is accelerated using an under-relaxation method given by [21, 23]

$$\begin{Bmatrix} \{u^{k+1}\} \\ \{v^{k+1}\} \\ \{w^{k+1}\} \\ \{\theta^{k+1}\} \end{Bmatrix} = \varepsilon \begin{Bmatrix} \{u^{k}\} \\ \{v^{k}\} \\ \{w^{k}\} \\ \{\theta^{k}\} \end{Bmatrix} + (1-\varepsilon) \begin{Bmatrix} \{u^{k-1}\} \\ \{v^{k-1}\} \\ \{w^{k-1}\} \\ \{\theta^{k-1}\} \end{Bmatrix} \tag{48}$$

where the superscripts denote iteration number and where ε was chosen as 2/3 [21].

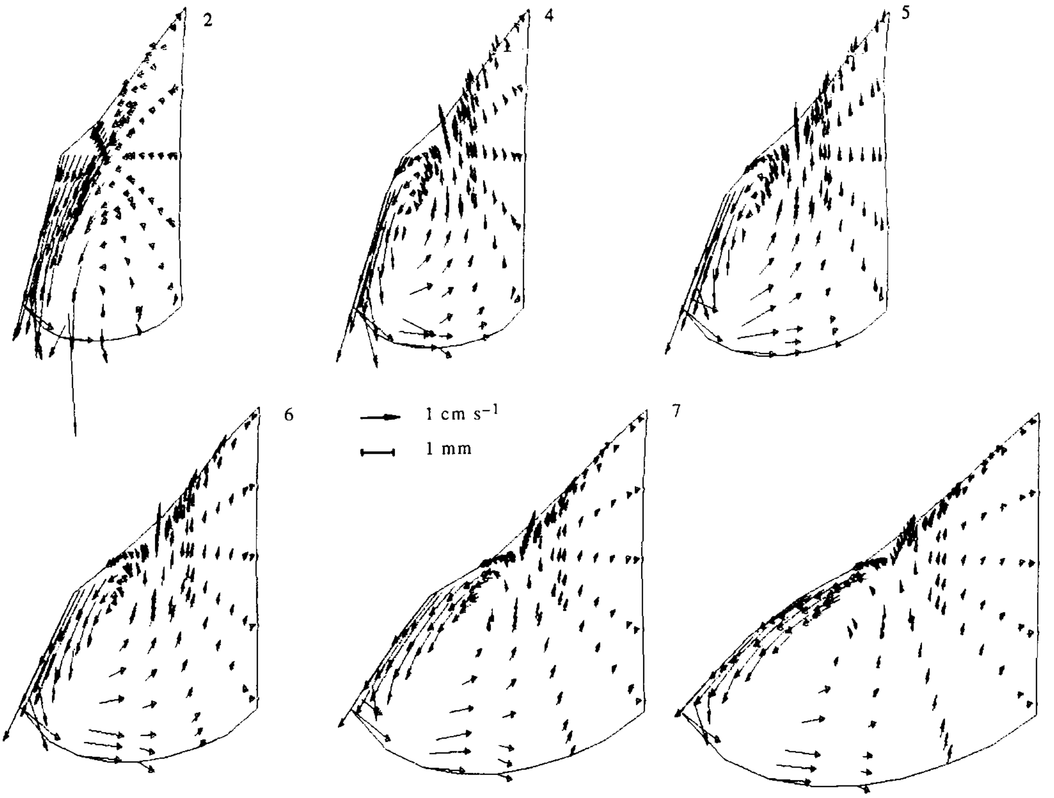

FIG. 6. Weld pool velocity fields in vertical cross-sections. $\tau_{jet}L_o/(|d\sigma/dT|(T_b - T_m)) = 10$, $Re = 10$, $Pe = 0.23$, $U = 1.5$ mm s^{-1}, $T_o = 30°C$, $d\sigma/dT < 0$.

A modified, out-of-core, frontal solver based on Hood's [24] program is used to solve the system of equations. The computations are performed on a CRAY X-MP and special buffering and asynchronous I/O features are implemented in order to optimize the larger amount of necessary I/O. For the calculations reported here, a mesh of 1088 brick elements, containing 1305 nodes is used in the fluid region. The upper capillary surface is divided into 64 quadratic surface elements (225 nodes), while the lower surface is divided into 32 quadratic surface elements (121 nodes). The mesh within the solid region is comprised of 240 brick elements containing 396 nodes. The characteristic Reynolds number is chosen based on a scaling argument presented below.

RESULTS

Weld pool shape

The effect of plate travel speed on weld pool shape is shown in Fig. 3. (In the following, we will refer to the extended region of the weld pool on the welded side of the plate as the *back* of the pool, and to the opposite side as the *front*.) As shown in Fig. 3(a), the weld pool is somewhat elliptical, and extends farther from the weld torch as the plate speed increases. In contrast, both the pool width and the distance between the keyhole and the pool front decrease with increasing plate speed. These results agree qualitatively with Hsu and Rubinsky's two-dimensional simulations [5]. Qualitatively, the results in Fig. 3(a) reflect the increasing importance of bulk heat transport in the travel direction relative to conduction in the x- and y-directions. Figure 3(b) shows the weld pool in cross section. The simulation indicates that pool sag, particularly in the lower-front and upper-back portions of the pool, increases significantly with plate speed.

The effect of ambient temperature on pool shape is shown in Fig. 4. This information is relevant to applications in low temperature environments either on Earth or in space. The results show that weld pool width and length decrease with decreasing ambient temperature. This behavior is physically reasonable since smaller boundary temperatures produce higher radial temperature gradients, implying that the characteristic distance between the keyhole and the fusion boundary will decrease. Differences in pool sag at the lower-front of the pool are not nearly as pronounced as in the case of varying plate velocity due to the relatively minor differences in pool radial width.

Pool temperature distribution

The temperature field within the weld pool is shown in Fig. 5. This result is representative of all the calculations that were performed. The simulated con-

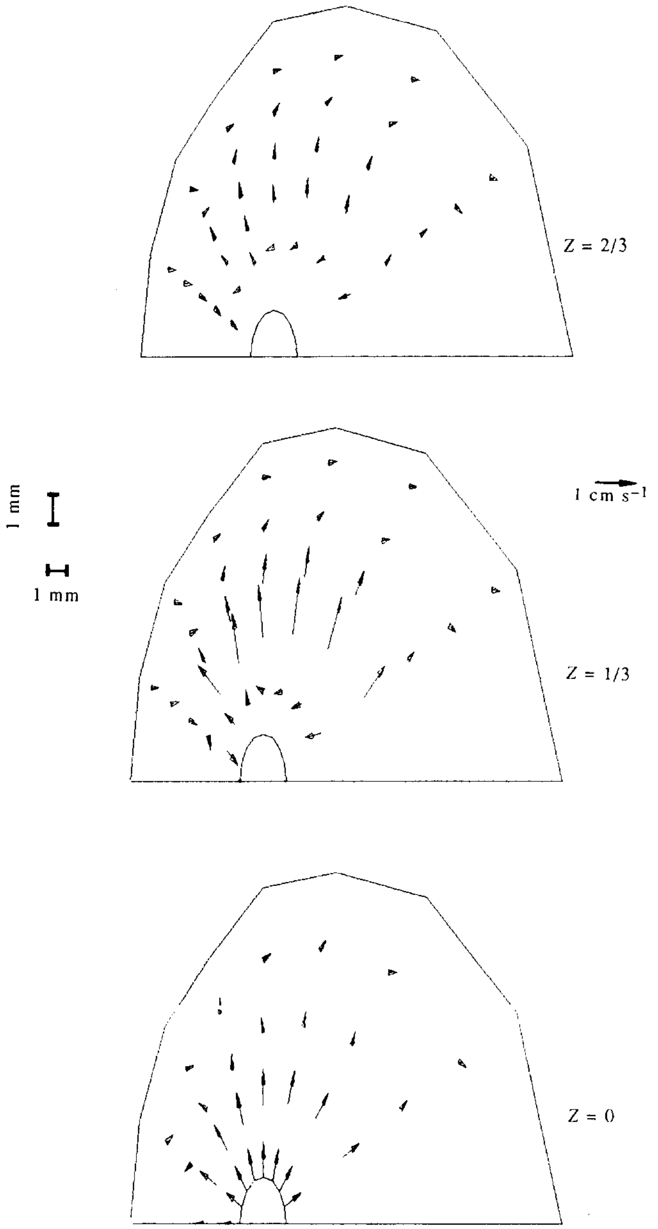

FIG. 7. Weld pool velocity fields in horizontal cross-sections. $\tau_{jet}L_0/(|d\sigma/dT|(T_b - T_m)) = 10$, $Re = 10$, $Pe = 0.23$, $U = 1.5$ mm s^{-1}, $T_0 = 30°C$, $d\sigma/dT < 0$.

ditions in this case are a 1.5 mm s^{-1} plate speed, and Peclet and Reynolds numbers of 0.23 and 10, respectively. The temperature solution shown corresponds to the conduction limit. The isotherms are essentially normal to the adiabatic, non-keyhole portions of the capillary surface and, in the vicinity of the keyhole, are parallel to the constant temperature keyhole interface. Similarly, neighboring isotherms are parallel to the fusion boundary.

Pool Reynolds number

It is important to note that the characteristic Reynolds number within the core region of PAW pools may not be as high as the 10^3–10^4 Reynolds numbers which often characterize other welding processes. This is due to two distinct features. First, a large free capillary surface forms the PAW pool's lower boundary, supporting the pool against dynamic and hydrostatic forces and effectively limiting the characteristic pool velocity scale. (Although a free capillary surface also comprises the lower boundary of laser and electron beam weld pools, the surface area in these instances is approximately an order of magnitude smaller than that in PAW [25].) Second, the PAW pool is subject to the force of an impinging plasma jet, a shear stress due to jet flow through the

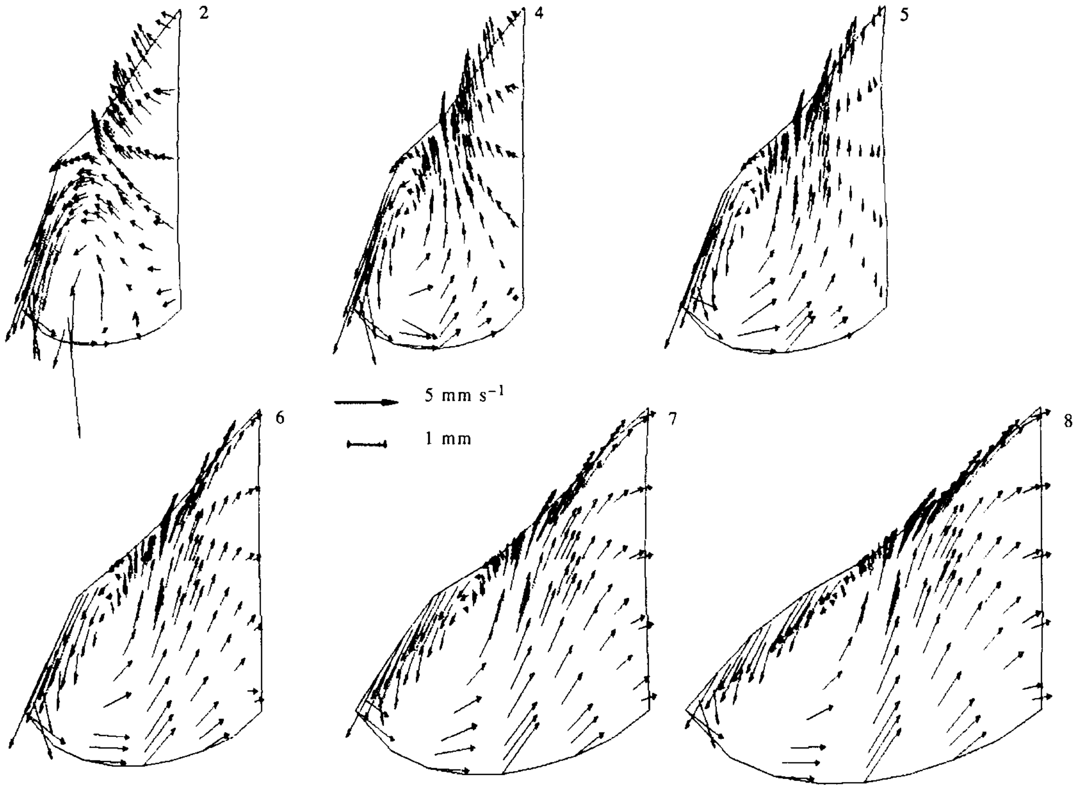

FIG. 8. Weld pool velocity fields in vertical cross-sections. $\tau_{\mathrm{jet}}L_o/(|d\sigma/dT|(T_b-T_m)) = 1$, $Re = 10$, $Pe = 0.23$, $U = 1.5$ mm s^{-1}, $T_o = 30$°C, $d\sigma/dT < 0$.

keyhole, and in many instances, the force due to an impinging shield gas.

An estimate of the characteristic PAW pool velocity and Reynolds number within the core region can be obtained by balancing all of the forces acting on the fluid region bounded by the plane $z = 0$ (see Fig. 2) and the lower capillary surface. Taking into account the hydrostatic head, the approximate force due to jet shear (conservatively estimated using the correlation in ref. [15]), the approximate force due to jet impingement, $\rho U_j^2\pi(r_t^2-r_b^2)$ (where ρ and U_j are characteristic jet densities and velocities and r_t and r_b are characteristic radii at the top and bottom of the keyhole), and assuming that the liquid metal at the bottom of the pool flows normally into and then back out of the control surface at $z = 0$ (as indicated by the simulated results), we find (by balancing against the upward acting surface tension force) that the characteristic velocity within the pool, U_p, could range from approximately 1 mm s^{-1} to 1 cm s^{-1}, depending on the assumed characteristic contact angle. (Note that due to the thinness of the thermocapillary-induced boundary layer, the corresponding dynamic pressure contribution is negligible.) Thus, for stainless steel, the corresponding characteristic core Reynolds number lies in the range $7 < U_pL_o/\nu < 70$. Experimental data are needed to clarify this issue. In all simulations presented in this paper, Re is set equal to 10 and the Peclet number is set to 0.23. The magnitudes of the other relevant flow parameters are given in the captions.

Pool fluid flow

Figure 6 shows the flow field when the jet shear is 10 times larger than the characteristic surface tension stress, $|d\sigma/dT|(T_b-T_m)/L$ ($\tau_{\mathrm{jet}} = 1400$ N m^{-2}), and assumes that $d\sigma/dT$ is negative. This simulation corresponds to flow induced by relatively large plasma mass flow through the keyhole, and assumes that surfactants are absent on the upper and lower free capillary surfaces. These conditions could also arise when jet shear is of normal magnitude but surface tension driven flow is inhibited due to the presence of an oxide layer, for example. Flow in vertical cross-sections is dominated by a jet driven circulatory region. The maximum velocity on any given vertical cross-section is approximately 10 cm s^{-1} and is located near the keyhole surface at the bottom of the keyhole. The velocities in the front of the pool are on the order of 1–10 cm s^{-1} and are directed predominantly downward. In the back part of the pool, in the region outside the circulating cells, velocities are on the order of the plate travel speed (O (1 mm s^{-1})). As described below, relatively fast downward flow in the front of the pool will induce a horizontal counterflow (i.e. directed against the plate travel direction) as required

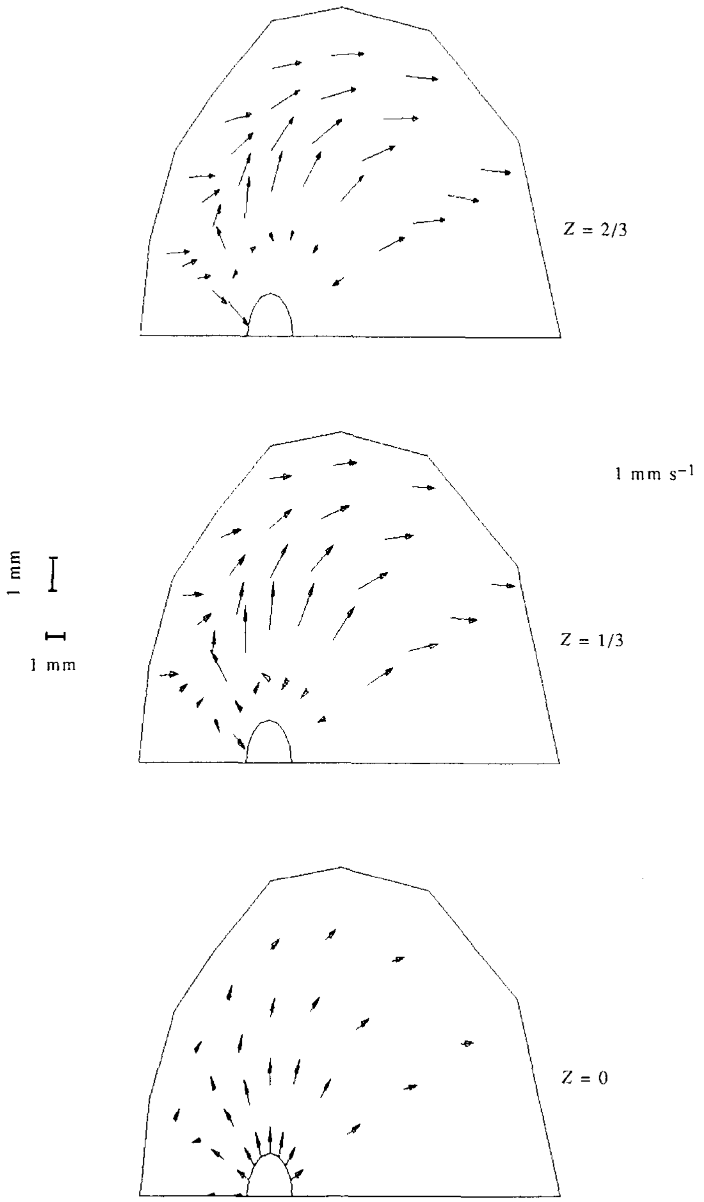

FIG. 9. Weld pool velocity fields in horizontal cross-sections. $\tau_{jet}L_o/(|d\sigma/dT|(T_b - T_m)) = 1$, $Re = 10$, $Pe = 0.23$, $U = 1.5$ mm s^{-1}, $T_o = 30°C$, $d\sigma/dT < 0$.

by continuity. A stagnation region is apparent near the top of the keyhole, produced by competition between jet shear and the radially outward acting thermocapillary stress. The velocities take on the boundary velocity along the fusion boundary, as is apparent in the various cross-sections.

The flow within various horizontal 'slices' through the pool are shown in Fig. 7. Since few element nodes lie on any given horizontal plane within the pool, horizontal velocity components at nodes lying on or within 0.5 mm of a given horizontal plane are shown (i.e. the slices are 1 mm thick). As shown, in the lower part of the pool the flow near the keyhole is generally directed radially outward. At all levels within the pool, the fluid tends to approach the fusion boundary and then turn toward the back of the pool, flowing somewhat parallel to the direction of plate movement. A weak (clockwise) circulating region appears to exist in the middle to upper reaches of the pool, as indicated in the top two horizontal cross-sections. As this flow approaches the keyhole, it tends to pass around the keyhole, against the direction of travel. Referring to Fig. 6, we see that the counterflow is induced by relatively high downward velocities in the front of the pool. The magnitudes of the horizontal velocity components near the fusion boundary and in the counterflow region are of the same order as the plate speed. Velocity magnitudes in the central regions are on the order of 1 cm s^{-1}.

Results somewhat similar to those found in the high jet shear case follow when the characteristic thermocapillary stress and jet shear are equal ($\tau_{jet} = |d\sigma/dT|(T_b - T_m)/L = 140$ N m^{-2}). See Figs. 8 and 9. As before, the maximum velocity in any given vertical cross-section occurs in the bottom portion of the pool. However, the maximum magnitude is only on the order of 1 cm s^{-1}, and in contrast to the first case, no predominantly downward flowing region exists (as in the cross-section in the upper left of Fig. 6). The velocities along the free capillary interfaces (Fig. 8) are more comparable to the velocities along the keyhole in this case, and the smaller velocities in general are evident when compared against the velocities along the fusion boundary. The velocities shown are absolute; thus velocity vectors point out of the free surfaces, and away from the keyhole, at angles that depend on the angle between the cross-section and the positive x-direction. Referring to Fig. 9, we see that the flow in horizontal sections is dominated by the plate's movement. The counterflow is minor and is confined to the immediate vicinity of the keyhole.

The effect of buoyancy on the PAW weld pool flow was investigated by holding the jet shear and surface tension at their characteristic values, and varying the Rayleigh number from 10^3 to 10^6 (the characteristic Rayleigh number for stainless steel in this problem is $O(10^4)$). It was found that the flow and temperature fields were essentially unaffected by buoyancy; this result is physically reasonable given the fact that the characteristic dynamic Bond number, $Bo_d = g\rho\beta L_o^2/|d\gamma/dT|$, is at most on the order of 0.1 (based on the values provided in Table 1).

CONCLUSIONS

Three-dimensional plasma arc weld pool shapes, temperature distributions and flow fields have been simulated under various conditions. Pool width decreases, while pool elongation increases with increasing plate travel speed. In contrast, pool width and length decreases with decreasing ambient temperature. A scaling argument suggests that in contrast to other welding processes, the characteristic PAW pool Reynolds number within the non-boundary layer core region is relatively small, due to the necessary balance between dynamic forces and surface tension. For the low Peclet number conditions considered here, weld pool heat transfer within the core is essentially due to conduction.

The pool flow is dominated by surface tension and jet shear forces. When the ratio of characteristic surface tension to jet shear is small, the flow in vertical cross-sections is dominated by a large circulation region in the center of the pool. Although a similar circulatory region exists when jet shear and surface tension are comparable, the velocities in this case are approximately an order of magnitude smaller than the high jet shear case. A stagnation region, apparent in vertical cross-sections, exists near the intersection of the upper capillary surface and the keyhole when the surface tension force is directed away from the keyhole. In both cases, a secondary, horizontal counterflow exists in the middle and upper reaches of the pool induced by relatively rapid, predominantly downward velocities in the front portion of the pool. Flow in horizontal planes is largely determined by the plate's motion when jet shear is of the same order of magnitude as the characteristic thermocapillary stress. Consistent with the small characteristic dynamic Bond number, buoyancy is found to have a negligible effect on weld pool flow.

Acknowledgements—This work was sponsored by NASA under grant NSA1-18686/GMM, and by a grant from Cray Research. The reviewer's comments on various aspects of this work are also acknowledged.

REFERENCES

1. A. C. Nunes, Jr., E. O. Bayless, Jr., C. S. Jones III, P. M. Munafo, A. P. Biddle and W. A. Wilson, Variable polarity plasma arc welding on the space shuttle external tank, *Welding J.* **63**, 27–35 (1985).
2. J. C. Metcalfe and M. B. C. Quigley, Heat transfer in plasma arc welding, *Welding J.* **54**, 99s–103s (1975).
3. Y. F. Hsu and B. Rubinsky, Transient melting of a metal plate by a penetrating plasma arc, *ASME J. Heat Transfer* **109**, 463–469 (1987).
4. R. G. Keanini and B. Rubinsky, Plasma arc welding under normal and zero gravity, *Welding J.* **69**, 41–50 (1990).
5. Y. F. Hsu and B. Rubinsky, Two-dimensional heat transfer study on the keyhole plasma arc welding process, *Int. J. Heat Mass Transfer* **31**, 1409–1421 (1988).
6. M. C. Tsai and S. Kou, Electromagnetic-force-induced convection in weld pools with a free surface, *Welding J.* **69**, 241s–246s (1990).
7. J. Dowden, N. Postacioglu, M. Davis and P. Kapadia, A keyhole model in penetration welding with a laser, *J. Phys. D: Appl. Phys.* **20**, 36–44 (1987).
8. S. Kou and D. K. Sun, Fluid flow and weld penetration in stationary arc welds, *Metall. Trans.* **16A**, 203–212 (1985).
9. S. Kou and Y. H. Wang, Weld pool convection and its effect, *Welding J.* **65**, 63s–70s (1986).
10. C. L. Chan, J. Mazumder and M. M. Chen, Perturbation model of three-dimensional thermocapillary convection in laser melt pool, paper 86-WA/HT-90, presented at the ASME Winter Annual Meeting, Anaheim, CA, December (1986).
11. T. Zacharia, A. H. Eraslan and D. K. Aidun, Modeling of non-autogenous welding, *Welding J.* **67**, 18s–27s (1988).
12. T. Zacharia, A. H. Eraslan and D. K. Aidun, Modeling of autogenous welding, *Welding J.* **67**, 53s–62s (1988).
13. C. L. Chan, R. Zehr, J. Mazumder and M. M. Chen, Three-dimensional model for convection in laser weld pool, *Proceedings of the Third Conference on Modeling and Control of Casting and Welding Processes*, Santa Barbara, CA, January (1986).
14. M. J. Tomsic and C. E. Jackson, Energy distribution in keyhole mode plasma arc welds, *Welding J.* **53**, 109s–115s (1974).
15. B. D. Hunn and R. J. Moffat, Radiative heat transfer

from a plasma in a tube flow, *Int. J. Heat Mass Transfer* **17,** 1319–1328 (1974).

16. S. Kou, Simulation of heat flow during the welding of thin plates, *Metall. Trans. A* **12A,** 2025–2030 (1981).
17. G. M. Oreper, T. M. Eager and J. Szekeley, Convection in arc weld pools, *Welding J.* **62,** 307s–312s (1983).
18. T. W. Eager and N.-S. Tsai, Temperature fields produced by traveling distributed heat sources, *Welding J.* **62,** 346s–355s (1983).
19. S. Ostrach, Low-gravity fluid flows. In *Annual Review of Fluid Mechanics* (Edited by M. V. Van Dyke, J. V. Wehausen and J. L. Lumley), Chap. 13. Annual Reviews, Palo Alto (1982).
20. D. H. Pelletier and J. A. Schetz, Finite element Navier–Stokes calculation of three-dimensional turbulent flow near a propeller, *AIAA J.* **24,** 1409–1416 (1986).
21. J. N. Reddy, Penalty-finite-element analysis of 3-D Navier–Stokes equations, *Comp. Meths Appl. Mech. Engng* **35,** 87–106 (1982).
22. R. A. Brown, Finite-element methods for the calculation of capillary surfaces, *J. Comp. Phys.* **33,** 217–235 (1979).
23. S.-W. Kim and R. A. Decker, Velocity–pressure integrated versus penalty finite element methods for high-Reynolds number flows, *Int. J. Numer. Meths Fluids* **9,** 43–57 (1989).
24. P. Hood, Frontal solution program for unsymmetric matrices, *Int. J. Numer. Meths. Engng* **10,** 379–399 (1976).
25. J. F. Lancaster, Ed., *The Physics of Welding*, pp. 271–276. Pergamon Press, New York (1984).